

# **Microstructural Evolution and Formation Mechanism of the Halo Ring in Resistance Spot Welding of a 3G Advanced High Strength Steel**

Dileep Chandran Ramachandran <sup>a,1</sup>, Adib Salandari-Rabori <sup>a</sup>, Andrew Macwan <sup>b</sup>, Elliot Biro <sup>a</sup>

<sup>a</sup> Centre for Advanced Materials Joining, Department of Mechanical & Mechatronics Engineering, University of Waterloo, Waterloo, Ontario N2L 3G1, Canada.

<sup>b</sup> ArcelorMittal Global Research, 1390 Burlington Street East, Hamilton, ON L8N 3J5, Canada.

---

<sup>1</sup> Corresponding author: *Dileep Chandran Ramachandran*

Centre for Advanced Materials Joining, Department of Mechanical & Mechatronics Engineering,  
University of Waterloo, Waterloo, Ontario, Canada N2L 3G1

E-mail: [dcramachandran@uwaterloo.ca](mailto:dcramachandran@uwaterloo.ca)

## **Abstract**

The microstructure of the halo ring has been studied in quenched and partitioned (Q&P) steel resistance spot welds. The TEM and EBSD characterizations revealed the presence of an upper bainitic microstructure in the halo ring of the three-sheet stack-up welds. Stacking faults accompanied by nano-twins were identified surrounding the cementite. Diffusion of carbon towards the molten weld pool during solidification led to the formation of bainite at the fusion boundary, triggered the localized softening.

**Keywords:** Advanced High Strength Steels; Resistance Spot Welding; Halo ring; Microstructure; TEM

Resistance spot welding (RSW) of advanced high-strength steels (AHSS), particularly those with extended welding times, are susceptible to fusion boundary (FB) failure where the crack propagates through a transient softened zone known as a halo ring [1,2]. Recent research indicates that third-generation (3G) advanced high-strength steels, such as quenched and partitioned (Q&P) steel, exhibit considerable sensitivity, particularly when spot-welded to steels with a different chemical composition [3-5]. Although numerous studies [1,2,6-9] have been conducted to investigate the formation and mitigation of the halo ring, the microstructural evolution in this region remains poorly understood.

Various investigations indicate that the softening phenomenon at the FB adversely impacts the failure mode of the spot welds thereby it promotes low energy failures [1,2,7-12]. To effectively mitigate the effect of this localized softening, a fundamental understanding of the halo microstructure and its characteristics is required. There are limited studies dealing with the microstructure and mechanism of halo formation. Li et al. [12] examined a DP 590 steel spot weld and anticipated that C depletion from the boundary to the grain interior possibly led to halo formation, though they lacked evidence for this claim. Sherepenko et al. [1,11,13] investigated resistance spot weldability of a 22MnB5 steel and proposed a mechanism for halo formation where  $\delta$  ferrite formed in the FB due to the prolonged isothermal soaking of the fusion zone (FZ) in the peritectic region. They supported their theory with evidence of carbon depletion in the FB through carbon mapping from phase-field simulations. Mohamadizadeh et al. [10] proposed that various solutes, including carbon and other alloying elements, diffuse from the solid heat-affected zone (HAZ) into the molten weld pool, potentially being a key factor in halo formation. They also proposed that solute partitioning could result in the formation of softer lower-carbon martensite adjacent to the FB, creating the halo ring. Lee et al. [14], on the other hand, examined the spot weldability of 15B22 hot-stamped steel, discovered that the halo consisted of soft ferrite, aligning with Sherepenko et al.'s [1,11,13] observations. Additionally, Zhang et al. [15] explored the spot weldability of Q&P 980 steel and observed a strong Mn depletion at the FB. They proposed that the decrease in hardness near the fusion zone is aligned with this phenomenon. However, despite their findings, Zhang et al. [15] failed to characterize the microstructure and propose a possible halo formation mechanism. Recently, Manladan et al. [7] identified a lath martensite structure in the halo ring, hypothesizing that the halo ring formed due to the macro-segregation of C and other alloying elements from the austenite to the weld pool. Despite numerous attempts to unveil the formation

mechanism and microstructure of the halo ring, the studies suffer from a lack of in-depth characterizations and analysis of formation mechanisms. Accordingly, a fundamental understanding of the halo ring is essential in the scientific community to mitigate this transient softening region, improving the post-welded properties of the resistance spot welds. Therefore, in this study, we conducted a fundamental thorough analysis of the halo ring microstructure and proposed a formation mechanism by using the state of art electron microscopy; electron backscattered diffraction (EBSD) and transmission electron microscopic (TEM) analysis.

In the present study, two 1.2 mm thick Q&P 980 steel samples were resistance spot welded, with a 1.5 mm interstitial-free (IF) steel sheet in the middle (three-sheet stack up). The nominal composition of the Q&P980 steel is Fe-0.23C-2.01Mn-1.05Si-0.22(Cr+Mo+Ti+Nb), and for the IF steel, it is Fe-0.002C-0.083Mn-0.004Si-0.08(Cr+Mo+Ti+Nb). The three-sheet stack-ups underwent resistance spot welding with a long welding time (470 ms) at its  $I_{\max}$  current. RSW was carried out using a medium-frequency direct current (MFDC) transformer with a C-type gun and a Rexroth Bosh weld controller. Other welding parameters are kept constant and were reported elsewhere <sup>[4]</sup>. The microstructure of the Q&P steel primarily consists of a combination of ferrite, martensite, tempered martensite, and retained austenite. A comprehensive characterization of the microstructure has been previously reported in earlier studies <sup>[4,5]</sup>. The microstructure of the halo ring was analysed using scanning electron microscopy (SEM) and electron backscattered diffraction in a JEOL JSM 7000F microscope. Transmission electron microscopic analysis was conducted on the focussed ion beam (FIB) milled samples extracted from the halo region using a Talos 200 TEM at an accelerating voltage of 200 keV.

An SEM image of the weld illustrating the interphase between Q&P and IF steel, with a distinctive halo ring on the Q&P steel side is shown in [Figure 1a](#). Details from the areas of the halo and HAZ, enclosed by the black rectangle, are shown in the inverse pole figure (IPF) map in [Figure 1b](#). The IPF map reveals that the halo ring is composed of coarse grains with relatively homogeneous microstructure and no evident lath or packet boundaries, which is in contrast to the lath martensitic structure observed in the HAZ. It has been reported that long welding time induces grain growth in the microstructure surrounding the weld nugget <sup>[16]</sup>. The width of the halo varies throughout the cross-section since the cooling rate significantly affects its formation. The average width of the halo ring is approximately 30  $\mu\text{m}$  near the sheet-sheet interphase (red arrows in [Figure](#)

1a) and it varies to  $\sim 150 \mu\text{m}$  near the electrode imprint region. In other words, the cooling rate is higher, leading to an earlier arrest of nugget growth [17] in the electrode imprint area compared to the sheet-sheet interphase, which leads to the formation of a wider halo. Moreover, as seen in Figure 1b, it is evident that all the microstructural constituents within an individual grain of halo share similar crystallographic orientations. This implies that the microstructural constituents in that specific location have undergone transformation from a common parent grain [18].

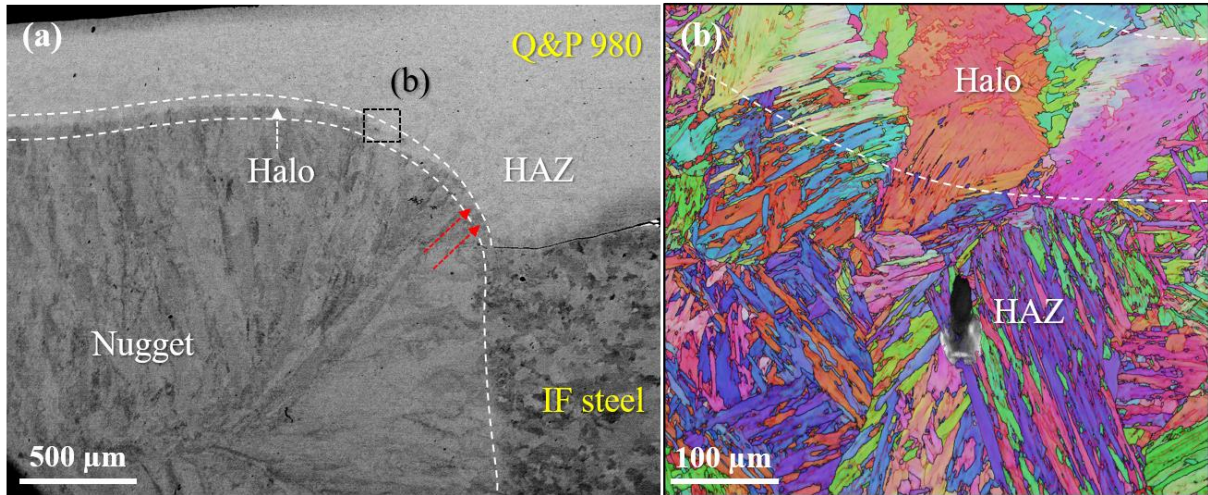


**Figure 1:** Microstructure of the spot weld three sheet stack up: (a) SEM cross-sectional micrograph of the weld and (b) EBSD IPF map of halo ring taken from the area shown in (a).

In-depth microstructural characterization of the halo ring using TEM is shown in Figure 2. The area from where the sample was extracted and the extracted sample are shown in Figure 2a. By analyzing the morphology from the TEM bright field image (Figure 2b), it can be seen that the microstructure of the halo consisted of an upper bainitic structure (no carbides were found in the ferrite matrix). It was observed that dislocation pile-ups and structures were not consistent throughout the structure, with some scatter pile-ups at initial pre-austenitic grain boundaries (PAGs). A selected area diffraction (SAD) pattern was extracted from the circle shown in Figure 2b and is depicted in Figure 2c. The interpretation of the SAD pattern shows that the microstructure consists of ferrite and cementite. The ferrite has an  $[112]_{\alpha} \parallel [011]_c$  orientation relationship with cementite, however, our findings did not align with these commonly reported orientation relationship like Bagaryatsky, and Pitsch-Petch [19]. To gain deeper insight, dark field TEM images were taken by isolating one spot (d in Figure 2c) from the other reflections. The reflection from the ferrite pattern shown in Figure 2d, confirms the presence of bainitic ferrite microstructure in

the halo ring, and the other reflection (see [Figure 2c](#)) confirms the presence of cementite as shown in [Figure 2g](#). The HAADF-STEM images were captured by placing the bainitic ferrite microstructure in the [111] zone axis, and the interplanar (d) spacing was measured using Image J software, as shown in [Figure 2e](#) and [f](#), respectively. The calculated d spacing was 2.04 Å, which shows good agreement with the d spacing of the ferrite along the (110) plane. Similarly, the HAADF-STEM image and its corresponding d spacing calculation of the cementite are shown in [Figure 2h](#) and [2i](#), respectively. The observed d spacing was 2.13 Å, which can be interpreted as cementite.

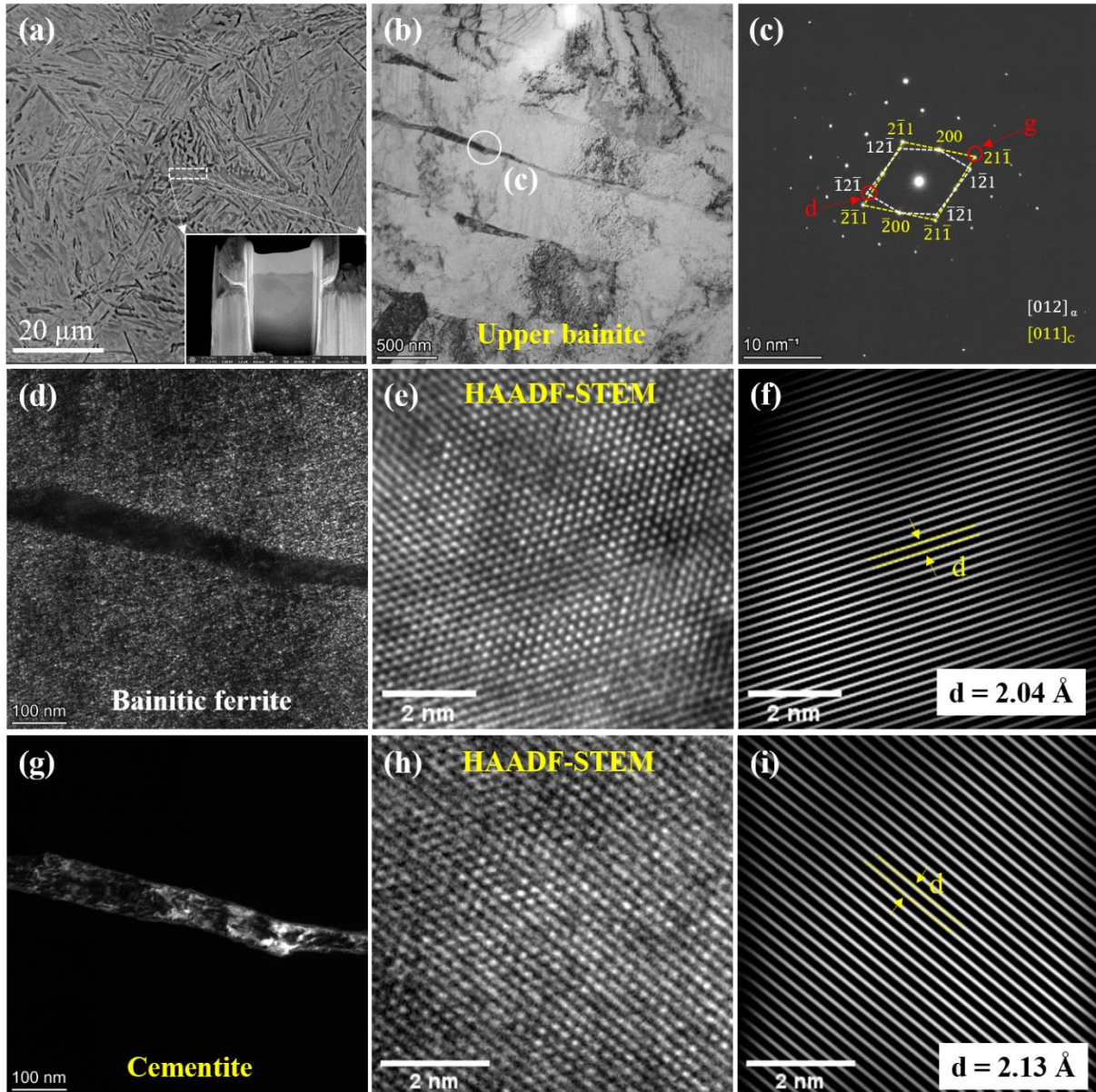


**Figure 2:** (a) FIB area and the sample (b) bright field image of the halo microstructure, (c) SAD pattern extracted from the white circle mentioned in (b), (d) dark field image of the bainitic ferrite by isolating the BCC reflection, (e) HAADF-STEM image of the ferrite in the  $[111]$  zone axis, (f) calculation of its d spacing, (g) dark field image of the cementite by isolating the corresponding reflection, (h) HAADF-STEM image of the cementite in the  $[011]$  zone axis, and (i) calculation of its d spacing.

Electron energy loss spectroscopy (EELS) map was employed to gain a deeper insight into the chemical nature of the halo ring microstructure. [Figure 3a](#) displays a representative TEM micrograph featuring the halo ring and the regions from which EELS maps were derived. EELS

maps depicting the distribution of carbon, iron, manganese, and silicon are presented in [Figure 3b-e](#), respectively. These maps reveal higher carbon content in the cementite region, confirming the microstructure as upper bainite. Notably, no manganese and silicon were observed, given that the presence of silicon can impede cementite formation <sup>[20]</sup>. However, the fringe-like patterns are speculated to be stacking faults (SFs) adjacent to the cementite, denoted by white arrows in [Figure 3f](#), which was confirmed by HAADF-STEM images ([Figure 3g](#)). SFs could form in the materials due to either deformation, the presence of crystal imperfections, or during high temperature process <sup>[21]</sup>. In this case, these SFs are believed to have formed during heating and cooling cycles, as well as due to the residual stresses and phase transformations during the welding process. In addition, it has been known <sup>[22]</sup> that decreasing carbon content reduces the stacking fault energy, making their formation more likely. On the other hand, carbon is an austenite stabilizer and the reduction in the carbon content increases the chance of austenite phase transformation upon cooling, promoting SF formation <sup>[22–24]</sup>. Surprisingly, it can be seen that SFs first are formed adjacent to the carbides at low-carbon regions and then extended into carbide particles. Carbides are deformed through the movement of SFs. It is speculated that these SFs are the result of the thermal stresses due to the ease of formation. Therefore, their existence in the microstructure at low carbon regions (areas nearer cementite) and within cementite is proof for the formation of an upper bainitic microstructure.

For an in-depth analysis of the internal structures, a Fast Fourier Transform (FFT) was extracted from the HAADF-STEM images and analyzed, as illustrated in [Figure 3h](#). The FFT analysis confirms the presence of stacking faults containing a nano twin with slight atomic arrangement deviations ( $\sim 16^\circ$ ) of four layers, further supported by the inverse FFT analysis (see [Figure 3i](#)).

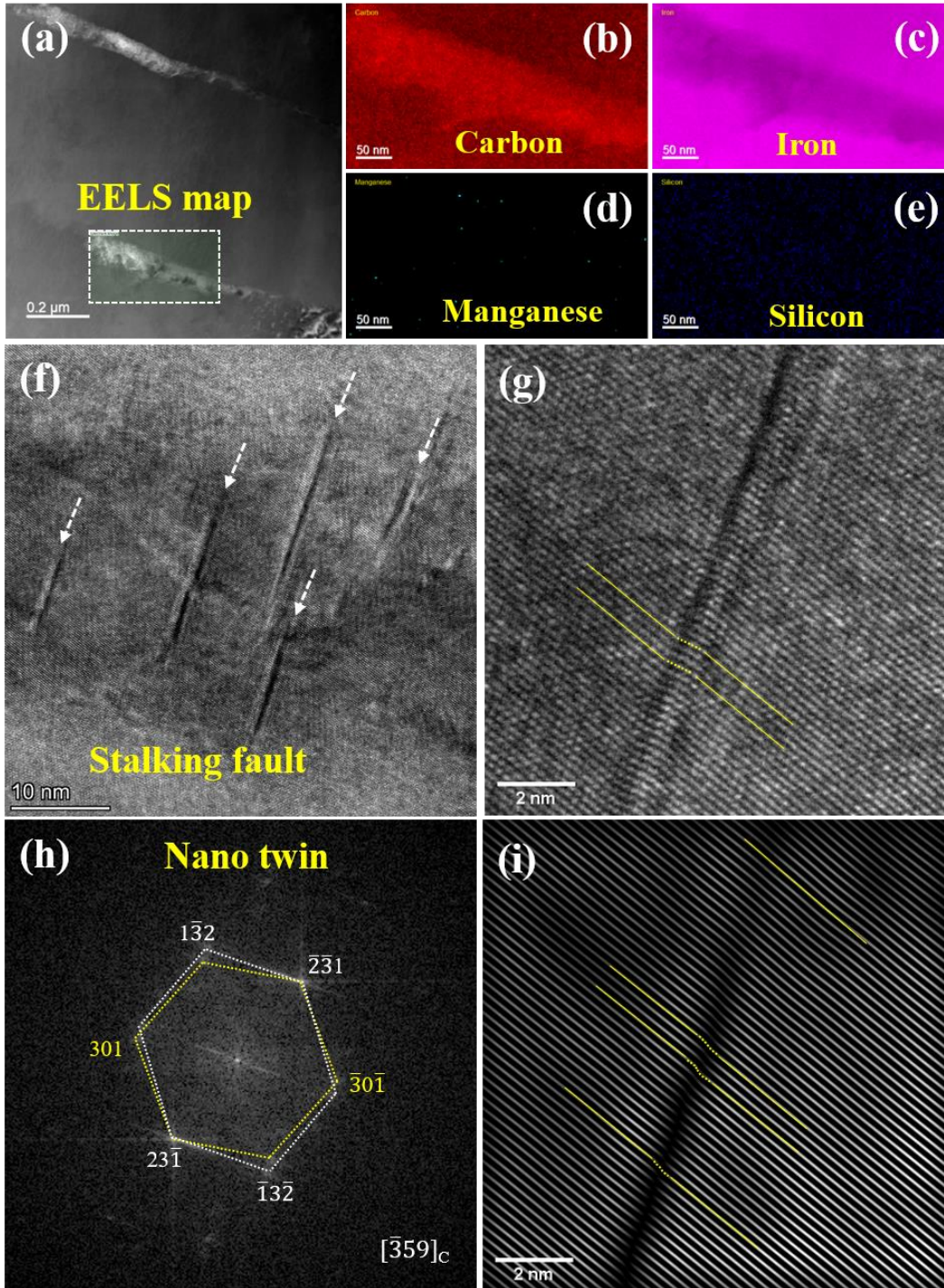


**Figure 3:** Electron energy loss spectroscopy analysis of the microstructure. (a) STEM image of the cementite, (b-e) carbon, iron, manganese, and silicon map, respectively, (f) presence of intrinsic stalking faults pointed out by white arrows, (g) HAADF-STEM image of the cementite showing a stalking fault in the middle, (h) FFT extracted from the (g) corresponding to  $[\bar{3}59]_c$  zone axis, (i) inverse FFT showing the change in arrangement of planes.

The microstructure identified in the carbon-depleted halo ring consists of the upper bainite. The schematic diagram in [Figure 4](#) summarizes the halo formation mechanism and progression of bainite microstructure formation from the initial austenite. In case of short welding time conditions, upon cooling, the austenite next to the FB transforms into the lath martensite <sup>[11]</sup>, as shown in [Figure 4b](#). This diffusion-less transformation occurs when a medium or high-carbon steel undergoes resistance spot welding under a single-pulse welding current with a short welding time <sup>[4]</sup>. This can be associated with the rapid cooling rate during the RSW process following the welding period. Consequently, the time available for the interplay between heat generation and heat dissipation at the FB is inadequate to form the halo ring. In contrast, when RSW are made with a prolonged welding time (470 ms) at welding currents (~0.1 to 0.3 kA) less than expulsion current, nugget growth reaches its maximum (approximately around 200 ms). Subsequently, the following ~270 ms, the FB experiences a cooling, which is dominated by heat dissipation through the electrodes. In other words, during later welding stages, after approximately 200 ms at  $I_{\max}$  current in this study <sup>[4]</sup>, the FB temperature decreases below the steel's solidus temperature, during the welding time itself, contributing to the equiaxed grain structure <sup>[4]</sup>. The extent of this drop in temperature gradient towards the center of the fusion zone depends on the welding time. As a result, there is carbon diffusion from the FB to the molten metal during solidification, driven by the elevated activity at the FZ attributed to its higher temperature <sup>[25]</sup>. This, in turn, leads to the transformation of the low-carbon region in the FB into bainite, as illustrated in [Figure 4c](#).

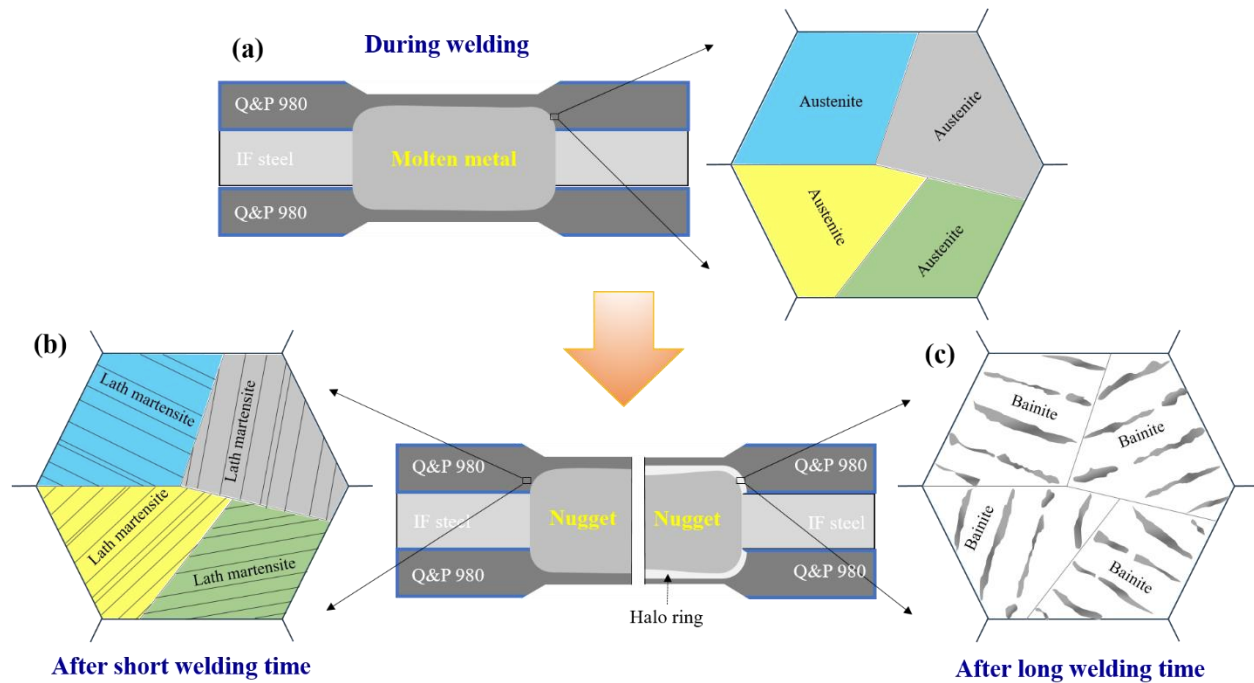


Figure 4: Schematic diagram showing (a) formation of austenite during the welding process, (b) transformation of austenite into martensite during cooling after a short welding time (c) transformation of austenite into bainite after a long welding time.

To summarize, a systematic TEM investigation disclosed that the microstructure within the halo ring is characterized by bainitic ferrite accompanied by needle-like cementite, specifically identified as upper bainite. This was further substantiated through high-resolution TEM (HRTEM) analysis, focusing on d-spacing and EELS mapping. Additionally, stacking faults and nano-twins were identified adjacent to the cementite, confirming the bainitic nature of the halo microstructure.

## Acknowledgments

The authors would like to acknowledge the financial support from the ArcelorMittal Dofasco G.P. in Hamilton, Canada, and the Natural Sciences and Engineering Research Council (NSERC). The electron microscopy was performed at the Canadian Centre for Electron Microscopy (also supported by NSERC and other government agencies).<sup>i</sup>

## Disclosure statement

The authors report there are no competing interests to declare.

## References

- 1 O. Sherepenko and S. Jüttner: *Weld. World*, 2019, vol. 63, pp. 151–9.
- 2 A. Mohamadizadeh, E. Biro, and M. Worswick: *Sci. Technol. Weld. Join.*, 2020, vol. 25, pp. 556–63.
- 3 B. Figueredo, D.C. Ramachandran, A. Macwan, and E. Biro: *Weld. World*, 2021, vol. 65, pp. 2359–69.
- 4 D.C. Ramachandran, B. Figueredo, O. Sherepenko, W. Jin, Y. Do Park, and E. Biro: *J. Manuf. Process.*, 2022, vol. 75, pp. 320–30.
- 5 D.C. Ramachandran, O. Timothy Betiku, M. Shojaee, A. Salandari-Rabori, A.R. Midawi, J.-U. Kim, R. Bakhtiari, A. Macwan, and E. Biro: *Mater. Charact.*, 2023, vol. 206, p. 113383.
- 6 O. Sherepenko, A. Mohamadizadeh, A. Zvorykina, M. Worswick, E. Biro, and S. Jüttner: *J. Mater. Sci.*, 2021, vol. 56, pp. 14287–97.
- 7 S.M. Manladan, Y.J. Jang, and Y. Do Park: *J. Mater. Res. Technol.*, 2023, vol. 24, pp. 4756–61.
- 8 D.C. Ramachandran, A. Salandari-Rabori, A.R.H. Midawi, A. Macwan, and E. Biro: *ISIJ Int.*, 2024, vol. 64, pp. 1178–84.

- 9 T. Taniguchi, T. Mizutani, H. Horikawa, S. Furusako, and S. Kodama: *J. Manuf. Process.*, 2024, vol. 117, pp. 1526–6125.
- 10 A. Mohamadizadeh, E. Biro, and M. Worswick: *72nd IIW Annu. Assem. Int. Conf.*
- 11 O. Sherepenko, A. Mohamadizadeh, A. Zvorykina, M. Worswick, E. Biro, and S. Jüttner: *J. Mater. Sci.*, 2021, vol. 56, pp. 14287–97.
- 12 Y.B. Li, D.L. Li, S.A. David, Y.C. Lim, and Z. Feng: *Sci. Technol. Weld. Join.*, 2016, vol. 21, pp. 555–63.
- 13 O. Sherepenko, O. Kazemi, P. Rosemann, M. Wilke, T. Halle, and S. Jüttner: *Metals (Basel)*, DOI:10.3390/met10010010.
- 14 H.T. Lee and Y.C. Chang: *Metals (Basel)*, 2020, vol. 10, pp. 1–17.
- 15 Y. Zhang, W. Xu, G. Zhang, W.U. Tao, and S. Yang: *Metall. Mater. Trans. A* 2021, 2022, pp. 1–16.
- 16 O.T. Betiku, D.C. Ramachandran, A. Ghatei-kalashami, C. DiGiovanni, O. Sherepenko, H. Ghassemi-Armaki, and E. Biro: *J. Mater. Process. Technol.*, 2023, vol. 320, p. 118122.
- 17 S.P. Murugan, K. Mahmud, C. Ji, I. Jo, and Y. Do Park: *Weld. World*, 2019, vol. 63, pp. 1613–32.
- 18 E.J. Seo, L. Cho, Y. Estrin, and B.C. De Cooman: *Acta Mater.*, 2016, vol. 113, pp. 124–39.
- 19 H. Wang, X. Zhang, D. Yan, C. Somsen, and G. Eggeler: *Nat. Commun.* 2018 91, 2018, vol. 9, pp. 1–7.
- 20 D. V. Edmonds, K. He, F.C. Rizzo, B.C. De Cooman, D.K. Matlock, and J.G. Speer: *Mater. Sci. Eng. A*, 2006, vol. 438–440, pp. 25–34.
- 21 J. Mola and B.C. De Cooman: *Metall. Mater. Trans. A Phys. Metall. Mater. Sci.*, 2013, vol. 44, pp. 946–67.

- 22 J. Xiong, H. Zhang, F. Nie, F. He, J. Yang, Z. Hu, Z. Wen, H. Zhao, and X. Yuan: *Met. Mater. Int.*, 2022, vol. 28, pp. 1639–49.
  - 23 B. Sun, A. Kwiatkowski da Silva, Y. Wu, Y. Ma, H. Chen, C. Scott, D. Ponge, and D. Raabe: *Int. Mater. Rev.*, 2023, vol. 68, pp. 786–824.
  - 24 L.E. Kar’Kina, T.A. Zubkova, and I.L. Yakovleva: *Phys. Met. Metallogr.*, 2013, vol. 114, pp. 234–41.
  - 25 M.L. Huang and L. Wang: *Metall. Mater. Trans. A Phys. Metall. Mater. Sci.*, 1998, vol. 29, pp. 3037–46.
-